Mm/sub-mm Bolometer Based on Electron Heating in Narrow-gap Semiconductor

V. Dobrovolsky, F. Sizov *, V. Zabudsky, N. Momot
Institute of Semiconductor Physics of the Ukrainian National Academy of Sciences,
Kiev-03028, Nauki Av., 41,
Tel: +380-44-5256296, Fax: +380-44-5251810,
* Email: sizov@isp.kiev.ua.

Abstract: Direct detection mm/sub-mm wave warm-carrier bipolar narrow-gap $Hg_{1-x}Cd_xTe$ semiconductor bolometers that can be used as picture elements in THz sensitive arrays, are considered. The response of $Hg_{1-x}Cd_xTe$ warm-electron bolometers was measured in ν=0.037-1.54 *THz* frequency range at T=68-300 *K*. Bipolar semiconductor warm-electron bolometer theoretical model was developed too. In the bolometer considered the electromagnetic wave propagates in semiconductor waveguide, heats electrons and holes there, creates their excess concentrations, as well as, the electromotive forces. These effects cause the bolometer response voltage. Experimental results confirm the model main conclusions. Because of response time defined by carrier recombination time in HgCdTe layers (τ~10^{-8}-10^{-6} s) and the noise equivalent power that can reach $NEP_{300\ K}$ ~ 4×10^{-10} *W/Hz*$^{1/2}$ in mm-wave region, the arrays on the base of HgCdTe bolometers can make them promising option for active fast frame rate sensitive applications.

Keywords: Mm/sub-mm radiation, warm-carrier effect, narrow-gap semiconductor bolometer

doi: 10.11906/TST.033-054.2010.03.04

1. Introduction

Terahertz (THz) technologies now received increasing interest for scientific and commercial applications (e.g., imaging, security, biological, drugs and explosion detection, gases fingerprints, etc.) (see, e.g., [1-3]) and these technologies frequently need relatively simple room temperature or not deeply cooled (T≥80 *K*) broadband direct detection detectors.

The majority of highly sensitive mm and sub-mm detectors operating at sub-liquid He temperatures are mainly used for astronomical applications (see, e.g., [4]). A variety of new THz detectors (the latter ones also mainly deeply cooled to T<1 *K*) were created during last years (for references see, e.g. [4, 5]). Except well known traditional uncooled mm and sub-mm detectors with room temperature noise equivalent power NEP~10^{-8}-10^{-10} *V/Hz*$^{1/2}$, which hardly can be assembled into real time imaging mm and sub-mm arrays (see, e.g., [5, 6]), recently were proposed several new type uncooled direct detection detectors (see, e.g., [7-10]) which can be easily assembled into arrays and used for real-time imaging.

One of the goals of this investigation was to develop not deeply cooled (T≥80 *K*) and relatively fast (with response time up to τ~50 *ns*) direct detection bolometer on the base of $Hg_{1-x}Cd_xTe$ (MCT) narrow-gap semiconductor, which can be assembled into arrays, and which is widely used, e.g., for IR large arrays manufacturing [11].

THz radiation range is frequently treated now as the spectral region within ν~(0.1-10) *THz* (λ~(3 *mm*-30 μm)) (see, e.g., [2]), thus partly overlapping with mm and sub-mm wavelength bands. And, because of it, frequently both these notions are used as equal ones.

In most absorption mm and sub-mm spectrometers with moderate resolution, are used traditional broad-band both uncooled and moderately cooled detectors. Among them are bolometers, Schottky diodes, piezoelectric detectors, Golay cells, etc. Except Schottky diodes most of broad-band mm and sub-mm uncooled detectors are relatively slow (response time τ_r>10 *ms*) and can't operate at lower temperatures to increase their sensitivity. The advantage of uncooled detectors, in spite of their relatively low sensitivity, lies in their room temperature operability in wide frequency band. Their noise equivalent power (NEP) is within NEP~(10^{-8}-10^{-10}) $W/Hz^{1/2}$ (see, e.g., [5]) Their main advantage lies in the relative operation simplicity without the need of adjustment in wide frequency band.

MCT has been developed over the past 50 years. Its optical, physical and electrical properties in the IR wave bands are well understood. The band-gap of MCT can be adjusted by varying the ratio of HgTe to the amount of CdTe in the particular MCT composition and is equal to $E_g \approx 0.083$ *eV* for $x \approx 0.2$ at T=77 *K* [11]]. As the material for creation of THz-detectors, $Hg_{1-x}Cd_xTe$ was tried to be used in receivers based on superlattices and heterojunctions [12, 13].

The possibility of bolometer creation that is sensitive in mm and sub-mm wavelengths region and that is based on the effect of free electrons heating in semiconductors was initiated in 1961 [14] and shortly hot electron bolometer (HEB) based on bulk n-InSb operating at liquid helium temperature was created [15]. Today electron type conductivity InSb or Ge bolometers are among sensitive devices and reach noise equivalent power NEP~2×10^{-13}-3×10^{-17} $W/Hz^{1/2}$ at T~4.2-0.3 *K*. With temperature increase their sensitivity drops quickly.

The possibility to use electron heating by electromagnetic wave in bipolar semiconductor layer for fabrication of THz/sub-THz bolometers was shown in [16]. MCT is a potential material for semiconductor HEB manufacturing because of narrow gap, high values of electron mobility μ_n and relatively small electron energy relaxation time τ_{nE} and free electron lifetime τ (for example, at $x \approx 0.2$ lifetime τ~50 *ns* and τ~20 *ns* for *p*-type layers at 300 and 77 *K*, respectively [11]).

In this paper warm-electron direct detection bolometers on the base of MCT bipolar narrow-gap semiconductor for THz and sub-THz region is considered. Their response in the 0.037-1.54 *THz* radiation frequency region is researched in *T*=(68-300) *K* temperature range.

2. Bolometer design and model assumptions

General model applied to narrow-gap MCT semiconductor warm-electron bolometer was developed for its schematic shown in Fig. 1. Here the thin layer of bipolar semiconductor with concentrations of donors N_d and acceptors N_a, respectively, is a sensitive element with the thickness a_1, the width a_2 and the distance a_3 between the metal contacts which serve as antennas. The width a_2 is greater than the thickness a_1 and electron and hole characteristic lengths too. Voltage U is applied to bolometer, R_{load} is a loading resistance.

From the antenna the electromagnetic wave $E_w \sim \exp(i\omega t)$, where i and $\omega=2\pi\nu$ are the imaginary unit and the frequency, respectively, enters the sensitive element, propagates in it as in a waveguide, and, as a result of charge carrier heating, changes electron and hole concentrations and causes the electromotive (emf) forces. E_w-field action creates electrons

and holes currents j_{wn} and j_{wp}, respectively, and therefore heats the carriers. Heating causes the addititional currents of electrons j_{nh} and holes j_{ph}, and due to this, the electric field E_h, as well as the electrons n_h and holes p_h excess concentrations. Both the carrier excess and the emf cause the bolometer response voltage. The radiation can enter and through the free surface at x=0 too. For the latter case a bolometer model is developed in [16]. But, comparison with the experiment have shown, that the antenna introduces much larger radiation power, compared to the power introduced through the free surface of sensitive layer.

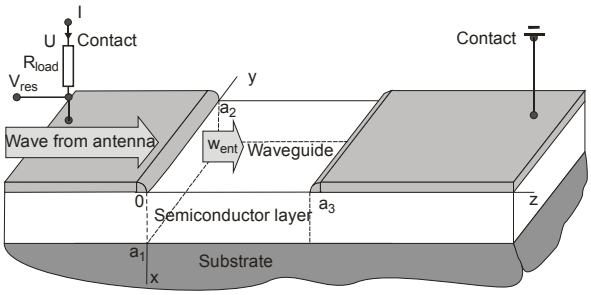

Fig.1 Bolometer schematic configuration.

Considered is the mm/sub-mm warm electrons bolometer on the base of thermodiffusion electron-hole pair flow in narrow-gap bipolar semiconductor or semimetal. If the flow transfers pairs from the sample region with high generation pairs rate to the region with slow recombination rate, then the number of free carriers in semiconductor layer between the contacts rises and its resistance decreases. And, vice-versa, if the pairs are transferred from the sample region with slow pair generation rate to the region with the high pair recombination rate, the number of free carriers decreases and the bolometer resistance decreases. Simultaneously, with resistance changes, nonuniform distribution of carriers temperature and their concentration cause the thermoelectromotive and Dember electromotive forces, respectively.

Changing the experimental conditions (e.g., changing the sample temperature, type of carriers and their concentration), because of the competition of the efects mentioneed, one can observe the resistance increase, or its decrease, and even the “zero” response under the radiation.

The resistance changes both the types of the electromotive forces that can be used to get the bolometer response voltage and, as it is shown both theoretically and experimentally, they can be noticeable in the temperature region of bipolar conductivity for narrow-gap semiconductor (T~80-300 K), and thus, mm/sub-mm direct detection bolometers can be designed on their base.

2.1 Warm electrons and holes

Concentrations, mobilities, effective masses, impulses and energy relaxation times of electrons and holes, and carrier lifetime are designated as n and p, μ_n and μ_p, m_n and m_p, τ_n and τ_p, τ_{En} and τ_{Ep}, and τ, respectively. It is assumed that the times $\tau_{n,p}$ and $\tau_{En,p}$ are independent on the electron/hole energy. Introduced are the temperatures of electrons T_n and holes T_p and, because of the assumption $m_n << m_p$, the energy interchange at the electron-hole

collisions is neglected. Being limited to the case of warm electrons (as the electric fields in the electromagnetic waves are small in the spectral regions under consideration), only quantities of the second order of smallness with respect to electric field and the lower order will be taken into account.

Further, expressions for electrons motion are written. It is assumed that $\mu_n=e\tau_n/m_n$, and replacing in them $e\rightarrow -e$, where e is the electron absolute charge value, $n\rightarrow p$ and introducing hole mobility as $\mu_p=e\tau_p/m_p$ one can obtain the expressions for holes.

The total electron current density can be written as

$$\boldsymbol{j}_n = - en\boldsymbol{u}_n, \tag{1}$$

where $\boldsymbol{u}_n$ is the electron mean velocity. Let us assume that the applied bias voltage is zero, then the model quantities can be written in the form $q=q_o+q_w(t,x,z)+q_h(t,x,z)$. Here q_o is the value, when the electromagnetic wave is absent. The wave electric field $\mathbf{E}_w$ action, as well as the wave action due to electron heating, cause the terms q_w and q_h, respectively

$$\boldsymbol{E}= \boldsymbol{E}_w+ \boldsymbol{E}_h, \quad \boldsymbol{u}_n= \boldsymbol{u}_{nw}+ \boldsymbol{u}_{nh}, \quad \boldsymbol{j}_n= \boldsymbol{j}_{nw}+ \boldsymbol{j}_{nh}, \quad T_n = T_o + T_{nh}, \quad n=n_o+n_h. \tag{2}$$

The q_w term has the first order of smallness on the field $\mathbf{E}_w$, while term q_h has the second order of smallness, as the electron heating power quadratically depends on the field. The quantity T_{nh} is the electron temperature counted from the lattice temperature T_o.

2.2 Average time quantities

Average time quantities $\overline{q}(x,z)$ generate the bolometer response voltage

$$\overline{q}(x,z)=\frac{\omega}{2\pi}\int_0^{\frac{2\pi}{\omega}} q(t,x,z)\,\mathrm{d}t\,, \tag{3}$$

$$\overline{q}_w=0,\ \overline{q}_h\neq 0 \text{ and } \overline{\partial q/\partial t}=0.$$

The condition for excess electrons and holes pair is

$$\overline{n}_h = \overline{p}_h\,. \tag{4}$$

2.3 Conservation equations of electron impulse, energy and concentration

Expressions (5), (6) and (8) below are the conservation equations of the electron mean impulse (m_nu_n), energy ($3k_BT_n/2$) and concentration (n), respectively

$$\frac{d\boldsymbol{u}_n}{dt}=-\frac{e\boldsymbol{E}}{m_n}-\frac{\nabla(nk_BT_n)}{m_nn}-\frac{\boldsymbol{u}_n}{\tau_n}, \tag{5}$$

$$\frac{3}{2}k_{\mathrm{B}}\frac{\partial nT_n}{\partial t}+\nabla\cdot\boldsymbol{Q}_n-P_{n\mathrm{h}}=-\frac{3}{2}k_{\mathrm{B}}n\frac{T_{n\mathrm{h}}}{\tau_E}, \tag{6}$$

$$\boldsymbol{Q}_n=-\frac{5}{2}\frac{k_{\mathrm{B}}T_n}{e}\left(\boldsymbol{j}_n+k_{\mathrm{B}}\mu_n n\nabla T_{n\mathrm{h}}\right), \tag{7}$$

where $nk_{\mathrm{B}}T_n$, $\mathrm{k_B}$ and $\boldsymbol{Q}_n$ are the electron gas pressure, Boltzmann constant and energy flow density, respectively, and

$$\frac{\partial n_{\mathrm{h}}}{\partial t}=\frac{1}{e}\nabla\cdot\boldsymbol{j}_n-\frac{n_{\mathrm{h}}}{\tau}. \tag{8}$$

If $|\boldsymbol{u}_n|$ is considerably smaller than thermal electron velocity, then $d\boldsymbol{u}_n/dt\approx\partial\boldsymbol{u}_n/\partial t$.

2.4 Semiconductor waveguide

Maxwell's equations

$$\nabla\times\boldsymbol{H}_{\mathrm{w}}=\varepsilon_{\mathrm{o}}\varepsilon_{\mathrm{L}}\frac{\partial\boldsymbol{E}_{\mathrm{w}}}{\partial t}+\boldsymbol{j}_{\mathrm{w}},\qquad \nabla\times\boldsymbol{E}_{\mathrm{w}}=-\mu_{\mathrm{o}}\mu_{\mathrm{L}}\frac{\partial\boldsymbol{H}_{\mathrm{w}}}{\partial t},\qquad \nabla\cdot\boldsymbol{H}_{\mathrm{w}}=0 \tag{9}$$

describe the wave propagation. Here ε_{o}, μ_{o} and ε_{L} are the electric and magnetic constants, and the semiconductor lattice relative permittivity, respectively. The magnetic permeability $\mu_{\mathrm{L}}=1$, $\varepsilon_o\mu_o=1/c^2$, where c is the light velocity in vacuum, $\boldsymbol{j}_{\mathrm{w}}=\boldsymbol{j}_{n\mathrm{w}}+\boldsymbol{j}_{p\mathrm{w}}$. If $\nu<1/\tau_{\mathrm{M}}$, where τ_{M} is the Maxwell relaxation time, the wave does not create the space charge and Poisson equation transforms into equation $\nabla\cdot\boldsymbol{E}_{\mathrm{w}}=0$.

The metal contact conductivity is much higher than the semiconductor one. Both this fact and the field tangential component continuity allow to assume an equality $E_{\mathrm{w}y}=0$ in semiconductor at its boundary with the contact. This condition at the radiation entrance causes the *TM*-wave in the sensitive layer. To find its field in the layer is possible only numerically.

At the same time, the layer region $0\le z\le a_3$, placed out of the contacts, is possible to be considered as a waveguide, and the fields there can be written as

$$\boldsymbol{E}_{\mathrm{w}}=\boldsymbol{E}_{\mathrm{a}}(x)\exp\left[i(\omega t-k_{\mathrm{c}}z)\right],\qquad \boldsymbol{H}_{\mathrm{w}}=\boldsymbol{H}_{\mathrm{a}}(x)\exp\left[i(\omega t-k_{\mathrm{c}}z)\right], \tag{10}$$

where $\boldsymbol{E}_{\mathrm{a}}(E_{\mathrm{ax}},0,E_{\mathrm{az}})$ and $\boldsymbol{H}_{\mathrm{a}}(0,H_{\mathrm{ay}},0)$ are the field amplitudes, $k_{\mathrm{c}}=k_{\mathrm{r}}+ik_{\mathrm{i}}$ is the wave vector, $k_{\mathrm{r}}>0$, $k_{\mathrm{i}}<0$. The radiation absorption coefficient equals $2|k_{\mathrm{i}}|$, and for $a_3\gtrsim 1/2|k_{\mathrm{i}}|$ the wave reflection at the contact at $z=a_3$ is negligible.

The electromagnetic field in the region $0\le z\le a_3$ can be described analytically and this layer region contributes mainly in the bolometer response voltage. Really, at radiation presence, the $\mathrm{E_{hz}}$ field component, and caused by the excess carriers change of z-component of the field, which the applied voltage U creates, both generate the response voltage (section 5). These

both field components are equal to zero at the contact boundaries and are small under the contacts. Taking these facts into account only portion $0 \le z \le a_3$ of semiconductor layer is considered.

In the warm electron approximation the electron heating power quadratically depends on electric field and for this approximation the linear in respect to field solution of Maxwell's equations with simple current expression

$$\boldsymbol{j}_{\mathrm{w}} = \sigma_{\mathrm{c}} \boldsymbol{E}_{\mathrm{w}} \tag{11}$$

is sufficient. Current (11) results from the current (1) after solution of Eq. (5) with the second term in the right part neglected for $\boldsymbol{u}_n = \boldsymbol{u}_{n\mathrm{w}} \sim \exp(i\omega t)$, $\boldsymbol{E} = \boldsymbol{E}_{\mathrm{w}} \sim \exp(i\omega t)$. In this current $\sigma_{\mathrm{c}} = \sigma - i\omega(\tau_n \sigma_n + \tau_p \sigma_p)$ is the complex conductivity, $\sigma = \sigma_n + \sigma_p$ is its real part, $\sigma_n = \sigma_{n\mathrm{o}} / (1 + \omega^2 \tau_n^2)$ and $\sigma_{n\mathrm{o}} = e\mu_n n_{\mathrm{o}}$ are the high frequency and equilibrium electron real conductivities, respectively, and $\mu_n = e\tau_n / m_n$. The electronic component of current $\boldsymbol{j}_{\mathrm{w}}$ is

$$\boldsymbol{j}_{n\mathrm{w}} = \sigma_n (1 - i\omega\tau_n) E_w . \tag{12}$$

Substitution of fields (10) and current (11) in two first equations (9) transforms them into $\nabla \times \boldsymbol{H}_{\mathrm{w}} = i\omega\varepsilon_{\mathrm{c}}\varepsilon_{\mathrm{o}} \boldsymbol{E}_{\mathrm{w}}$ and $\nabla \times \boldsymbol{E}_{\mathrm{w}} = -i\omega\mu_{\mathrm{o}} \boldsymbol{H}_{\mathrm{w}}$, where $\varepsilon_{\mathrm{c}} = \varepsilon - i\sigma / \omega\varepsilon_{\mathrm{o}}$ is the complex dielectric permittivity and $\varepsilon = \varepsilon_{\mathrm{L}} - (\tau_n \sigma_n + \tau_p \sigma_p) / \varepsilon_{\mathrm{o}}$ is its real part. The ε value depends on frequency and can be negative. Manipulation with the last formulae for the $\boldsymbol{E}_{\mathrm{w}}$ and $\boldsymbol{H}_{\mathrm{w}}$ yields the equation

$$\frac{d^2 H_{\mathrm{ay}}}{dx^2} - \frac{k_{\mathrm{c}}^2 c^2 - \omega^2 \varepsilon_{\mathrm{c}}}{c^2} H_{\mathrm{ay}} = 0 \tag{13}$$

and intercoupling

$$E_{\mathrm{ax}} = \frac{k_{\mathrm{c}} H_{\mathrm{ay}}}{\omega\varepsilon_{\mathrm{c}}\varepsilon_{\mathrm{o}}}, \qquad E_{\mathrm{az}} = -\frac{i}{\omega\varepsilon_{\mathrm{c}}\varepsilon_{\mathrm{o}}} \frac{dH_{\mathrm{ay}}}{dx}. \tag{14}$$

The boundary conditions $E_{\mathrm{ax}|x=0,a_1} = 0$ and $H_{\mathrm{ay}|x=0,a_1} = 0$ follow from an equality $j_{wx|x=0,a_1} = 0$, as well as, from Exps.(10), (11) and (14). For these conditions the solution of Eq.(13) can be written as

$$H_{\mathrm{ay}} = A \sin\left(\frac{m\pi x}{a_1}\right), \tag{15}$$

where A is the constant, $m = 1, 2 \ldots$. and $k_{\mathrm{c}}^2 = \omega^2 \varepsilon_{\mathrm{c}} / c^2 - m^2 \pi^2 / a_1^2$ is the dispersion equation. Solving this equation one can obtain

$$k_{\mathrm{r}}=\left(\frac{\omega^2\varepsilon}{2c^2}-\frac{m^2\pi^2}{2a_1^2}+\frac{1}{2}\sqrt{\left(\frac{m^2\pi^2}{a_1^2}-\frac{\omega^2\varepsilon}{c^2}\right)^2+\frac{\omega^2\sigma^2}{c^4\varepsilon_{\mathrm{o}}^2}}\right)^{\frac{1}{2}},\qquad k_{\mathrm{i}}=-\frac{\omega\sigma}{2c^2\varepsilon_{\mathrm{o}}k_{\mathrm{r}}}. \tag{16}$$

The conditions of the wave input into the waveguide specify the mode m of wave propagation. Comparison of the given by Exps. (14) and (15) the electric field components, with the electric field values found numerically, shows that for the bolometer design discussed $m = 1$.

Electron heating specific power equals to $P_{n\mathrm{h}}=\mathrm{Re}\boldsymbol{j}_{n\mathrm{w}}\cdot\mathrm{Re}\boldsymbol{E}_{\mathrm{w}}$. In the model developed, only its average time quantity (see Exp.(3)) is necessary. It can be calculated as $\overline{P}_{n\mathrm{h}}=\mathrm{Re}\left(\boldsymbol{j}_{n\mathrm{w}}^{*}\cdot\boldsymbol{E}_{\mathrm{w}}\right)/2$, where the symbol (*) signifies the complex conjugation. The radiation energy flow into the waveguide at z=0 equals to $\overline{w}_{\mathrm{ent}}=a_2\int_0^{a_1}\overline{S}_z(x,0)\,\mathrm{d}x$, where $\overline{\boldsymbol{S}}=\mathrm{Re}\left[\boldsymbol{E}_{\mathrm{w}}\times\boldsymbol{H}_{\mathrm{w}}^{*}\right]/2$ is the average time Pointing vector. Substitution of fields $\boldsymbol{E}_{\mathrm{w}}$ and $\boldsymbol{H}_{\mathrm{w}}$, obtained from Exps.(10), (14) and (15), into the $\overline{w}_{\mathrm{ent}}$ integral, interrelates constant A from Exp.(15) with flow $\overline{w}_{\mathrm{ent}}$. Use of this interrelation and substitution of current $\boldsymbol{j}_{n\mathrm{w}}$ (12) and $\boldsymbol{E}_{\mathbf{w}}$ in the above expression for the power $\overline{P}_{n\mathrm{h}}$ result into the following expressions

$$\overline{P}_{n\mathrm{h}}=\overline{P}_{n\mathrm{ho}}\exp(2k_{\mathrm{i}}z),\quad \overline{P}_{n\mathrm{ho}}=\frac{2\overline{w}_{\mathrm{ent}}\sigma_n\left[\left(m^2\pi^2-|k_{\mathrm{c}}|^2a_1^2\right)\cos^2\left(\frac{m\pi x}{a_1}\right)+|k_{\mathrm{c}}|^2a_1^2\right]}{a_1^3a_2\left(k_{\mathrm{r}}\varepsilon\varepsilon_{\mathrm{o}}\omega-k_{\mathrm{i}}\sigma\right)}. \tag{17}$$

2.5 Average temperature $\langle T_{n\mathrm{h}}\rangle$ and concentration $\langle n_{\mathrm{h}}\rangle$

Equation for the average time temperature $\overline{T}_{n\mathrm{h}}$ can be written as

$$\frac{\partial^2\overline{T}_{n\mathrm{h}}}{\partial x^2}+\frac{\partial^2\overline{T}_{n\mathrm{h}}}{\partial z^2}=\frac{\overline{T}_{n\mathrm{h}}}{L_{En}^2}-\frac{2}{5}\frac{e\overline{P}_{n\mathrm{h}}}{k_B^2T_{\mathrm{o}}\mu_n n_{\mathrm{o}}}, \tag{18}$$

where $L_{En}=\sqrt{5k_BT_{\mathrm{o}}\mu_n\tau_{En}/3e}$ is the electron cooling length. To obtain this equation, the quantities in Exps.(6)-(8) were taken as sums (2) and were averaged on time, in accordance with Exp. (3). Then in Eq.(6) the energy flow density $\overline{\boldsymbol{Q}}_{n\mathrm{h}}$ and quantity $\nabla\cdot\overline{\boldsymbol{j}}_{n\mathrm{h}}$, derived respectively from Exps. (7) and (8), were used. Finally, because of $\tau\gg\tau_{En}$ in the equation found for temperature $\overline{T}_{n\mathrm{h}}$, the term proportional to $\overline{n}_{\mathrm{h}}/\tau$, was neglected.

The average thickness quantities are thickness dependent

$$\langle q\rangle(z)=\frac{1}{a_1}\int_0^{a_1}\overline{q}(x,z)\,dx. \tag{19}$$

Decrease of the layer thickness a_1 in comparison with the distance a_3, $1/2\,|k_i|$ and the electron/hole characteristic lengths reinforces the simplification accuracy used.

Going away from the surfaces at x=0, a_1, according to Exp. (17), the electron heating becomes weaker. This allows to assume the equalities $\partial\overline{T}_{n\mathrm{h}}/\partial x_{|x=\delta}=\partial\overline{T}_{n\mathrm{h}}/\partial x_{|x=a_1-\delta}=0$, in which the value δ depends on the surface electron cooling intensity, and $\delta \lesssim L_{En}$. If such cooling is absent, then δ=0. Integration of the equation for $\overline{T}_{n\mathrm{h}}$ (18) across the layer under assumed conditions $\partial\overline{T}_{n\mathrm{h}}/\partial x_{|x=0,a_1}=0$ transforms it in equation for both the average time and thickness electron temperature $\langle T_{n\mathrm{h}}\rangle$:

$$\frac{d^2\langle T_{n\mathrm{h}}\rangle}{dz^2}=\frac{\langle T_{n\mathrm{h}}\rangle}{L_{En}^2}-\frac{\langle T_{n\mathrm{ho}}\rangle\exp(2k_{\mathrm{i}}z)}{L_{En}^2}, \tag{20}$$

where $$\langle T_{n\mathrm{ho}}\rangle=\langle P_{n\mathrm{ho}}\rangle\tau_{En}/c_{\mathrm{h}}\,, \tag{21}$$

and $c_{\mathrm{h}}=3k_{\mathrm{B}}n_{\mathrm{o}}/2$, $\langle P_{n\mathrm{ho}}\rangle=\overline{w}_{\mathrm{ent}}\sigma_n\left(m^2\pi^2+|k_{\mathrm{c}}|^2a_1^2\right)/\left[a_1^3a_2\left(k_{\mathrm{r}}\varepsilon\varepsilon_{\mathrm{o}}\omega-k_{\mathrm{i}}\sigma\right)\right]$ are the electron gas specific heat and the average electron heating input specific power, respectively. The condition used for $\partial\overline{T}_{n\mathrm{h}}/\partial x$ is valid, if $a_1 \lesssim L_{En}$ and $\partial\overline{T}_{n\mathrm{h}}/\partial x\approx 0$ across the layer. For an opposite inequality, this condition does not lead to an essential error, as the contribution of areas near the surfaces in the electron temperature formation is small.

The sense of characteristic temperature $\langle T_{n\mathrm{ho}}\rangle$ is the stationary electron temperature at homogeneous heating by power $\langle P_{n\mathrm{ho}}\rangle$.

Expression for electron current density

$$\overline{\boldsymbol{j}}_{n\mathrm{h}}=\sigma_{no}\overline{\boldsymbol{E}}_{\mathrm{h}}+k_{\mathrm{B}}\mu_n\left(T_{\mathrm{o}}\nabla\overline{n}_{\mathrm{h}}+n_{\mathrm{o}}\nabla\overline{T}_{n\mathrm{h}}\right) \tag{22}$$

follows from Exps.(1), (2) and (5). Exclusion of the field $\overline{\boldsymbol{E}}_{\mathrm{h}}$ from $\overline{\boldsymbol{j}}_{n\mathrm{h}}$, using expressions for the $\overline{\boldsymbol{j}}_{p\mathrm{h}}$ and (4), allows to write $\overline{\boldsymbol{j}}_{n\mathrm{h}}=\sigma_{no}\left[\overline{\boldsymbol{j}}_{\mathrm{h}}+k_{\mathrm{B}}\mu_p p_{\mathrm{o}}\nabla\left(\overline{T}_{n\mathrm{h}}+\overline{T}_{p\mathrm{h}}\right)\right]/\left(\sigma_{no}+\sigma_{po}\right)+eD_{\mathrm{amb}}\nabla\overline{n}_{\mathrm{h}}$, where $\overline{\boldsymbol{j}}_{\mathrm{h}}=\overline{\boldsymbol{j}}_{n\mathrm{h}}+\overline{\boldsymbol{j}}_{p\mathrm{h}}$ and $D_{\mathrm{amb}}=k_BT_{\mathrm{o}}\mu_n\mu_p\left(n_{\mathrm{o}}+p_{\mathrm{o}}\right)/\left(\sigma_{no}+\sigma_{po}\right)$ is the bipolar diffusion coefficient. Substitution of last current $\overline{\boldsymbol{j}}_{n\mathrm{h}}$ in Eq. (8) leads to the equation

$$\frac{\partial^2\overline{n}_{\mathrm{h}}}{\partial x^2}+\frac{\partial^2\overline{n}_{\mathrm{h}}}{\partial z^2}=\frac{\overline{n}_{\mathrm{h}}}{D_{\mathrm{amb}}\tau}-\chi\left[\frac{\partial^2\left(\overline{T}_{n\mathrm{h}}+\overline{T}_{p\mathrm{h}}\right)}{\partial x^2}+\frac{\partial^2\left(\overline{T}_{n\mathrm{h}}+\overline{T}_{p\mathrm{h}}\right)}{\partial z^2}\right], \tag{23}$$

Where $$\chi=\frac{n_{\mathrm{o}}p_{\mathrm{o}}}{T_{\mathrm{o}}\left(n_{\mathrm{o}}+p_{\mathrm{o}}\right)}\,. \tag{24}$$

Let us designate the recombination rates on surfaces x=0, a_1, effective carrier life time and effective bipolar diffusion length as $s_0, s_{a_1}, \tau_{\mathrm{ef}}$ and L_{D}, respectively, $1/\tau_{\mathrm{ef}}=1/\tau+\left(s_0+s_{a_1}\right)/a_1$, $L_{\mathrm{D}}=\sqrt{D_{\mathrm{amb}}\tau_{\mathrm{ef}}}$. The integration across the layer with the use of average thickness quantities

(19), as well as, the equalities $\overline{j}_{\mathrm{h}x|x=0,a_1}=0$, $\partial\overline{T}_{n\mathrm{h},p\mathrm{h}}/\partial x_{|x=0,a_1}$ =0 and $\overline{j}_{n\mathrm{h}x|x=0,a_1}=\pm e\cdot s_{0,a_1}\overline{n_{\mathrm{h}}}_{|x=0,a_1}$ transforms Eq. (23) in equation for the both average time and thickness excess electron concentration $\langle n_{\mathrm{h}}\rangle$

$$\frac{d^2\langle n_{\mathrm{h}}\rangle}{dz^2}=\frac{\langle n_{\mathrm{h}}\rangle}{L_{\mathrm{D}}^2}-\chi\frac{d^2\left(\langle T_{n\mathrm{h}}\rangle+\langle T_{p\mathrm{h}}\rangle\right)}{dz^2}. \tag{25}$$

This equation can be interpreted as the bipolar diffusion equation, in which $D_{\mathrm{amb}}\,\chi\,d^2\left(\langle T_{n\mathrm{h}}\rangle+\langle T_{p\mathrm{h}}\rangle\right)/dz^2$ is the electron-hole pair generation rate.

2.6 Distributions of $\langle T_{n\mathrm{h}}\rangle$ and $\langle n_{\mathrm{h}}\rangle$ along the waveguide

The solution of Eq. (20) is

$$\langle T_{n\mathrm{h}}\rangle=F\left[0,L_{En},\langle T_{n\mathrm{h}}\rangle(a_3),\langle T_{n\mathrm{h}}\rangle(0),z\right]+\langle T_{n\mathrm{ho}}\rangle\frac{F\left(k_{\mathrm{i}},L_{En},1,1,z\right)-\exp\left(2k_{\mathrm{i}}z\right)}{4k_{\mathrm{i}}^2L_{En}^2-1}, \tag{26}$$

in which $F\left(k,L,\alpha,\beta,z\right)=\left\{\alpha\exp(2ka_3)\sinh\left(z/L\right)+\beta\sinh\left[\left(a_3-z\right)/L\right]\right\}/\sinh\left(a_3/L\right)$. The solution of Eq. (25) is

$$\langle n_{\mathrm{h}}\rangle=\langle\eta_{n\mathrm{h}}\rangle+\langle\eta_{p\mathrm{h}}\rangle+F\left[0,L_{\mathrm{D}},\langle n_{\mathrm{h}}\rangle(a_3),\langle n_{\mathrm{h}}\rangle(0),z\right], \tag{27}$$

where

$$\begin{aligned}\langle\eta_{n\mathrm{h}}\rangle=&\frac{\chi\langle T_{n\mathrm{ho}}\rangle}{1-4k_{\mathrm{i}}^2L_{En}^2}\left[\frac{F\left(k_{\mathrm{i}},L_{\mathrm{D}},1,1,z\right)-F\left(k_{\mathrm{i}},L_{En},1,1,z\right)}{L_{En}^2/L_{\mathrm{D}}^2-1}+\frac{F\left(k_{\mathrm{i}},L_{\mathrm{D}},1,1,z\right)-\exp\left(2k_{\mathrm{i}}z\right)}{1-1/4k_{\mathrm{i}}^2L_{\mathrm{D}}^2}\right]\\&+\chi\frac{F\left[0,L_{En},\langle T_{n\mathrm{h}}\rangle(a_3),\langle T_{n\mathrm{h}}\rangle(0),z\right]-F\left[0,L_{\mathrm{D}},\langle T_{n\mathrm{h}}\rangle(a_3),\langle T_{n\mathrm{h}}\rangle(0),z\right]}{L_{En}^2/L_{\mathrm{D}}^2-1}\end{aligned}, \tag{28}$$

$\langle n_{\mathrm{h}}\rangle=\langle p_{\mathrm{h}}\rangle$. Only electron (hole) heating creates the $\langle\eta_{n\mathrm{h}}\rangle$+($\langle\eta_{p\mathrm{h}}\rangle$) summand in Eq.(27).

In Exps.(26) and (27) the quantities $\langle T_{n\mathrm{h}}\rangle(0)$, $\langle T_{n\mathrm{h}}\rangle(\mathrm{a}_3)$ and $\langle n_{\mathrm{h}}\rangle(0)$, $\langle n_{\mathrm{h}}\rangle(\mathrm{a}_3)$ are the values at the waveguide ends, which simultaneously are the contact boundaries. Intensive recombination on them allows one to accept

$$\langle n_{\mathrm{h}}\rangle(0)=\langle n_{\mathrm{h}}\rangle(a_3)=0. \tag{29}$$

Condition (29) transforms Exp.(27) into: $\langle n_h\rangle=\langle\eta_{nh}\rangle+\langle\eta_{ph}\rangle$.

For boundary value $\langle T_{n\mathrm{h}}\rangle(a_3)$ a condition similar to Exp.(29) is valid. However, near the input contact the electron temperature formation is other, than that $\langle T_{n\mathrm{h}}\rangle(a_3)$. Really, the

electron heating under this contact and cooling on its surface, both fix the temperature value in this case. Then, it can be written

$$\langle T_{nh}\rangle(0) = \gamma_n \langle T_{nho}\rangle,\ \langle T_{nh}\rangle(a_3) = 0, \tag{30}$$

where the introduced dimensionless temperature γ_n depends on the contact design. As it is clear from the $\langle T_{nho}\rangle$ definition in section 4.1, the γ_n can have values from zero up to several units. In general case $\gamma_n = \gamma_n(\nu, T_o)$.

2.7 Long layer approximation

Nearby the input contact the electron heating is the largest one. The opposite contact only reduces the $\langle T_{nh}\rangle$ and $\langle n_h\rangle$ values. Let's consider a long layer with $a_3 >> L_{En}, 1/2|k_i|, L_D$, when the influence of the opposite contact is negligible. Then Exp.(26) is reduced to the expression $\langle T_{nh}\rangle/\langle T_{nho}\rangle = \left\{\left[\exp(-z/L_{En}) - \exp(2k_i z)\right]/\left(4k_i^2 L_{En}^2 - 1\right)\right\} + \gamma_n \exp(-z/L_{En})$, in which the electron heating at $z > 0$ and boundary temperature $\langle T_{nh}\rangle(0)$ cause the first and second terms, respectively. For the high electron heating at the input contact the second term gives the temperature monotone decrease. If the second term is small there is the $\langle T_{nh}\rangle$ maximum. The $\langle T_{ph}\rangle/\langle T_{pho}\rangle$ expression for holes is similar to that one for electrons. Relationship $\langle T_{nho}\rangle/\langle T_{pho}\rangle = \mu_n \tau_{En}\left(1+\omega^2\tau_p^2\right)/\mu_p \tau_{Ep}\left(1+\omega^2\tau_n^2\right)$ follows from Exp. (21). This implies that usually the electron heating is stronger than the hole one, inasmuch as inequalities $\mu_n > \mu_p$, $\tau_{En} > \tau_{Ep}$ and $\tau_n > \tau_p$ are typical for semiconductors, and $\eta_{nh} > \eta_{ph}$.

Fig. 2 shows the η_{nh} concentration part distribution for the case $\gamma_n = 0$. Radiation increases the electron gas temperature and pressure in the region $0 < z \lesssim 1/2|k_i|$. This, and condition (4), cause the thermodiffusion electron-hole pair flow to the input contact. Intensive recombination on it decreases the pair concentration and their full number.

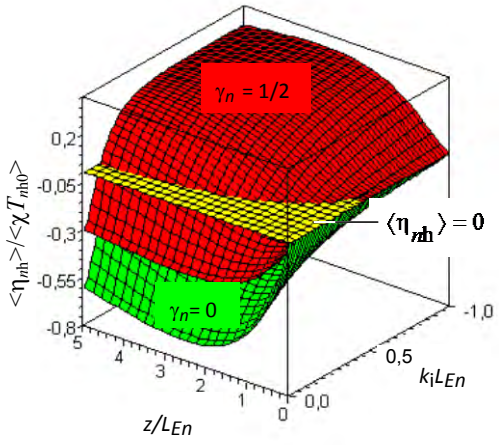

Fig. 2 Excess electron concentration $\langle \eta_{nh}\rangle$ (Exp. (28)) in units $\chi\langle T_{nho}\rangle$ (Exps. (21) and (24)) in the long semiconductor layer: $a_3 >> L_{En}$, $\frac{1}{2}|k_i|$, L_D, and $L_D = 10 \times L_{En}$.

The situation becomes more complicated, if $\gamma_n>0$. Then the high boundary electron temperature causes flow of the pairs, which are generated at the input contact, deep into the layer. This flow can increase the pair concentration and their full number (see dependence for γ_n =1/2 in Fig.2).

Thus, changing the experimental conditions (e.g., changing the sample temperature, type of carriers and their concentration), because of the competition of the effects mentioneed, one can observe the pair concentration decrease (and, thus, resistance increase), or its increase, and even the "zero" changes of pair concentration under the radiation which leads to "zero" response. All these features were observed experimentally in dependence of the bolometer temperature, free carrier concentrations and the majority carriers type of conductivity.

2.8 Components of the response voltage

In the region considered $0\le z\le a_3$ (Fig.1) the source U creates the voltage $V_{\rm ext}$, the electric field $\boldsymbol{E}_{\rm ext}(0,0,V_{\rm ext}/a_3)$, which is assumed weak, and the current density $\boldsymbol{j}_{\rm ext}=(\sigma_{no}+\sigma_{po})\boldsymbol{E}_{\rm ext}$. From Exps. (3) and (11) for $\boldsymbol{j}_{\rm ext}$ follows the additivity of the electron heating powers $\overline{\left(\boldsymbol{j}_{\rm ext}+{\rm Re}\boldsymbol{j}_{\rm w}\right)\cdot\left(\boldsymbol{E}_{\rm ext}+{\rm Re}\boldsymbol{E}_{\rm w}\right)}=\left(\sigma_{no}+\sigma_{po}\right)\boldsymbol{E}_{\rm ext}^2+\overline{P}_{n\rm h}+\overline{P}_{p\rm h}$. This implies that actions of the $\boldsymbol{E}_{\rm ext}$ and $\boldsymbol{E}_{\rm w}$ fields can be considered independently, and the results obtained earlier can be used at the voltage U switched on.

Let us designate the voltage $V_{\rm ext}$, if radiation is absent, as $V_{\rm exto}$ and its change by radiation as $\overline{V}_{\rm exth}$. For the circuit in Fig.1 the equality

$$U=V_{\rm exto}+\overline{V}_{\rm exth}+\int_0^{a_3}\langle E_{\rm hz}\rangle dz+\overline{I}R_{\rm load} \tag{31}$$

can be written. In it $\overline{V}_{\rm exth}+\int_0^{a_3}\langle E_{\rm hz}\rangle dz=V_{\rm res}$ is a voltage response. The current through the bolometer equals $\overline{I}=a_1a_2(j_{\rm extz}+\langle j_{\rm hz}\rangle)$, where current under radiation $\langle j_{\rm hz}\rangle=\langle j_{n\rm hz}\rangle+\langle j_{p\rm hz}\rangle$ can be found from Exps.(19) and (22). Substitution of $\langle j_{\rm hz}\rangle$ into current $\overline{I}$ and integration of the obtained expression on length a_3, with using of Eq. (31), result in the following sum

$$V_{\rm res}=V_{\rm D}+V_T+V_N. \tag{32}$$

In sum (32) the Dember emf ($V_{\rm D}$), the thermoelectromotive of warm electrons ($V_{\rm T}$) and the layer conduction changes due to excess carriers ($V_{\rm N}$), when condition (30) is applied, cause, respectively, the voltages

$$V_{\rm D}=\frac{a_1a_2k_{\rm B}T_{\rm o}\left(\mu_n-\mu_p\right)}{a_3}\times\frac{\langle n_{\rm h}\rangle(0)-\langle n_{\rm h}\rangle(a_3)}{1/R_{\rm load}+1/R_{\rm o}},$$

$$V_T=\frac{a_1a_2k_{\rm B}}{a_3e}\times\frac{\sigma_{no}\gamma_n\langle T_{n\rm ho}\rangle-\sigma_{po}\gamma_p\langle T_{p\rm ho}\rangle}{1/R_{\rm load}+1/R_{\rm o}}\ , \tag{33}$$

$$V_N = -\frac{a_1 a_2 e(\mu_n + \mu_p)}{a_3^2} \times \frac{N_h V_{exto}}{1/R_{load} + 1/R_o} \ .$$

Here $R_o = a_3 / [a_1 a_2 (\sigma_{no} + \sigma_{po})]$ is the equilibrium resistance and $N_h = \int_0^{a_3} \langle n_h \rangle dz$ is the full number of the excess electrons upon the unit of the layer cross-section square.

Further, the case close to practical situation of condition (29) and voltage $V_D = 0$ will be considered.

For $R_{load} >> R_o$ the voltage $V_T = k_B (\sigma_{no} \gamma_n \langle T_{nho} \rangle - \sigma_{po} \gamma_p \langle T_{pho} \rangle) / [e(\sigma_{no} + \sigma_{po})]$ is the thermoelectromotive. It arises in the semiconductor bulk, but not in the barrier. The electron heating is stronger, than the hole one and, usually, $V_T > 0$. However, if inequality $\sigma_{po} \gamma_p \langle T_{pho} \rangle > \sigma_{no} \gamma_n \langle T_{nho} \rangle$ takes place, the hole heating changes the sign of the V_T voltage.

Substitution $\langle n_h \rangle$ from exp. (27), at conditions (29) and (30), in $N_h = \int_0^{a_3} \langle n_h \rangle dz$ gives

$$N_h = N_{nh} + N_{ph}, \tag{34}$$

where $$N_{nh} = \int_0^{a_3} \langle \eta_{nh} \rangle dz = \frac{\chi \langle T_{nho} \rangle}{1 - 4k_i^2 L_{En}^2} \left\{ \frac{\Phi(L_D) - \Phi(L_{En})}{L_{En}^2 / L_D^2 - 1} + \frac{\Phi(L_D) + [1 - exp(2k_i a_3)]/2k_i}{1 - 1/4k_i^2 L_D^2} \right\} +$$
$$\gamma_n \chi \langle T_{nho} \rangle \times \frac{L_{En} \tanh(a_3/2L_{En}) - L_D \tanh(a_3/2L_D)}{L_{En}^2 / L_D^2 - 1}$$

and $\Phi(L) = L [1 + \exp(2k_i a_3)] \tanh(a_3/2L)$.

It is handy to write the voltage V_N (33) as the sum $V_N = V_b + V_\gamma$, in which the V_b component does not depend and V_γ one depends on dimensionless temperatures γ_n and γ_p at the waveguide input, respectively. Substitution of sum (34) into the voltage V_N allows one to obtain expressions for the V_b and V_γ. Carriers heating in the region $0 \le z \le a_3$ reduces their number and causes the voltage V_b. Generated at the input contact electrons and holes diffuse into this region and cause the voltage V_γ. If $V_{exto} > 0$, then $V_b > 0$ and $V_\gamma < 0$, and for $V_{exto} < 0$ the voltages V_b and V_γ signs are changed. In n-type semiconductor the hole heating is small compared to the electron one and, according to exps. (33) and (34), the relations $V_T \sim \langle T_{nho} \rangle$ and $V_b, V_\gamma \sim \chi \langle T_{nho} \rangle$ hold true. In p-type semiconductor the "light" electrons should play more important role and thus the voltages V_{res}, V_T, V_b and V_γ must be greater, than those ones in n-type semiconductor.

In Fig.3 shown are the relative response calculations on radiation frequency for n- and p-type MCT layers, the parameters of which are close to the samples experimentally investigated. One can see that according to calculations the response relatively weakly depends on frequency ν in the assumtion of the power introduced to the sensitive layer does not depend on ν (coupling efficiency does not depend on ν) and response is several times larger in p-type layers.

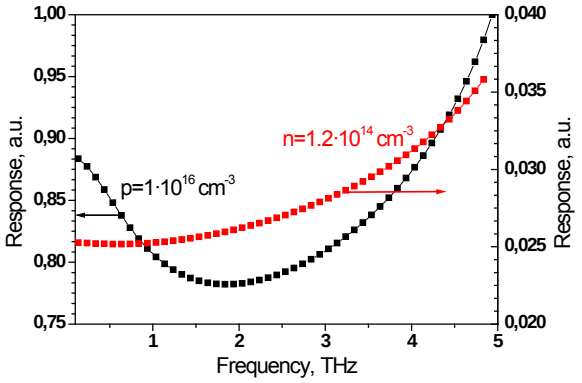

Fig. 3 Calculated response frequency dependencies of n- and p-type MCT bolometers.

The presented bolometer model is applicable if $a_1 > \lambda_n$, where λ_n is the electron wave length. In the temperature range T~(60-300) *K* in $Hg_{1-x}Cd_xTe$ layers with x~0.2 for electrons and light holes λ_n <0.2 *μm* (electron effective nasses $m_n<0.015 \cdot m_0$, where m_0 is free electron mass). When plotting different dependences only such T_o and a_1 values were used, for which an inequality $a_1/\lambda_n > 5$ and condition $\nu<1/\tau_M$, are valid.

Energy relaxation time at different temperatures T_o were estimated from expressions in [17] for polar optical scattering (they are $\tau_{En}\sim10^{-12}$ *s* and $\tau_{Ep}\sim10^{-13}$ *s*) and Debye temperature ~140 K [18]. The rest characteristics of $Cd_{0.2}Hg_{0.8}Te$ were taken from [11] ($\mu_n=9\cdot10^4\cdot(m_n\cdot T)^{-3/2}$ $cm^2/V\cdot s$, $m_n/m_0\approx0.071\cdot E_g$, where E_g is a temperature dependent band gap, $E_g(77K)\approx0.083$ *eV*, $E_g(300K)\approx0.1546$ *eV*). The electron carrier lifetime equals τ~2 *μs* for T_o<100 *K* [19] for similar samples and the temperature rise until 300 *K* reduces it to τ~30 *ns*. In p-type layers τ~20 *ns* (T<100*K*) and τ~50 *ns* (T~300*K*). Equilibrium electron n_o and hole p_o concentrations values were found according to statistics formulas.

In contrast to radiation frequency, the layer thickness a_1 should change strongly the k_i and $\langle P_{n\text{ho}}\rangle$ values. For example, the thickness a_1 rise from 1 to 10 *μm* reduces k_i and $\langle P_{n\text{ho}}\rangle$ quantities by more than one and three orders, respectively. Due to Exp.(21), strong dependence $\langle P_{n\text{ho}}\rangle = \langle P_{n\text{ho}}\rangle(a_1)$ causes such dependence $\langle T_{n\text{ho}}\rangle = \langle T_{n\text{ho}}\rangle(a_1)$ and responsivity should increase noticeably.

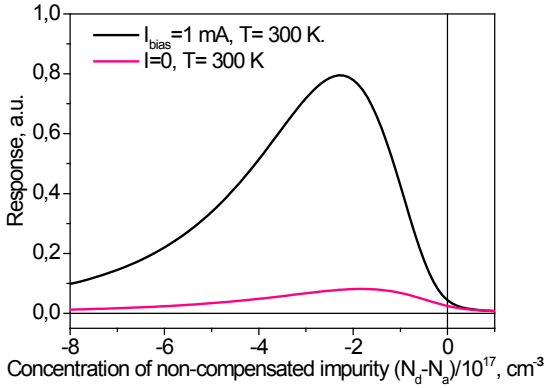

Fig. 4 Bolometer response calculated dependences as a function of impurity concentration.

The lattice temperature T_o variation weakly changes the k_i and $\langle P_{nho} \rangle$ values (less than by 30 % in the conditions under discussion). However, if the concentration dependence $n_o(T_o)$ is significant then, due to relation $\langle T_{nho} \rangle \sim 1/c_h \sim n_o(T_o)$ (see Exp. (21)), the dependence $\langle T_{nho} \rangle (T_o)$ is strong too. But change of conductivity type from *n*-type to *p*-type should lead to principle increase of sensitivity, which can be pronounced in certain range of hole concentrations (see Fig.4). The theory predicts better sensitivity for samples with *p*-type conductivity (see Fig.4 for theoretical estimations) that was confirmed experimentally (see Fig. 5).

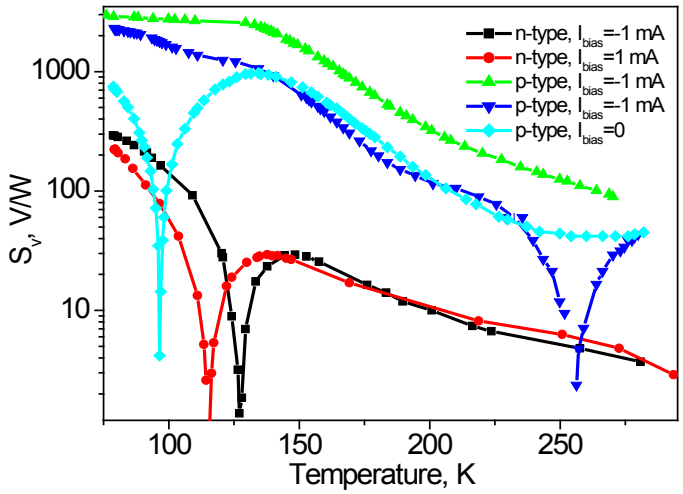

Fig. 5 Sensitivity temperature dependencies of n- and p-type MCT bolometers. ν=37.5 *GHz*, n(78 K)~$1.5 \cdot 10^{14}$ cm^{-3}, p(78 K)~$3 \cdot 10^{16}$ cm^{-3}, Electrical contact area S=$1.9 \cdot 10^{-3}$ cm^2. Radiation power at sample location W~40 $\mu W/cm^2 \times 1.9 \cdot 10^{-3}$ $cm^2 \approx 7.5 \cdot 10^{-8}$ *W*.

3. Comparison with experiment

Experimental results in the long layer approximation (see paragraph 2.7) confirm in general the temperature sensitivity dependencies of proposed detectors in wide spectral range at least from 0.037 to 1.58 *THz*. In Fig. 5 are shown the sensitivity temperature dependencies of n-type and p-type layers at ν≈37.5 *GHz*. p-type conductivity layer was obtained by annealing of n-type layer investigated. One can see pronounced difference in temperature dependencies and S_v values for these samples for radiation frequency ν=37.5 *GHz*. For p-type layer the sensitivity is several times higher. For this sample even at I_{bias}=0 the signal is substantial but the main contribution from generation-recombination noise is absent that gives the opportunity to get rather appropriate NEP values (for this sample at T≈130 *K* the estimations give NEP~10^{-12} $W/Hz^{1/2}$ and at T=300 *K* NEP~3×10^{-11} $W/Hz^{1/2}$), because the basic generation-recombination noise is absent at I_{bias}=0. When estimating S_v and NEP values the radiation power at the samples placement and antenna area (S=1.9×10^{-3} cm^2) were used.

The same relation is seen from the dependencies in Fig. 6 for radiation frequency ν=78 *GHz*, though the sensitivity is much less for the same samples compared to sensitivity at ν=37.5 *GHz* which seems is connected with frequency dependence of antennas coupling efficiency. Experimental results were obtained for detectors with non-optimized bolometer sizes and antennas design. Sensitivity should be greater with lowering of detector size and

optimized antenna. Estimating S_V and NEP values radiation power at the samples placement and antenna area (A=1.9×10^{-3} *cm*^{2}) were used.

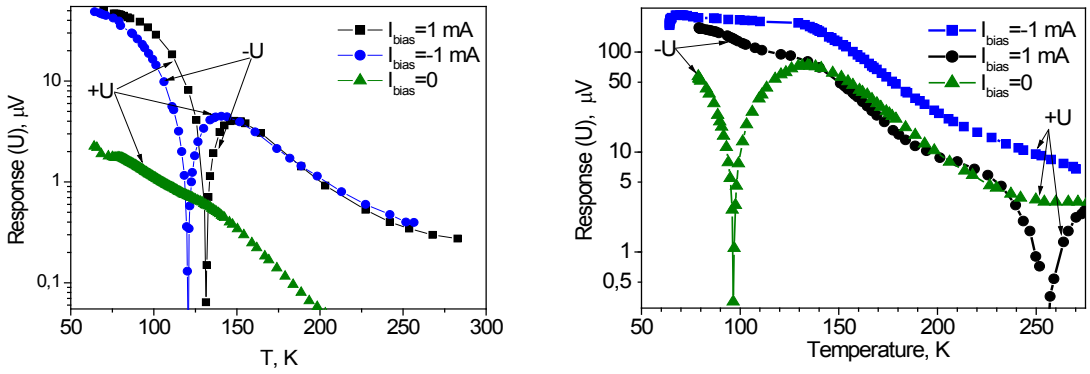

Fig. 6 Response of n-type (left) and p-type (right) $Hg_{0.8}Cd_{0.2}Te$ bolometer as a function of temperature. The frequency of incident radiation ν=78 *GHz*. The frequency of modulation f=360 *Hz*. Radiation flux density is W~4.5 *mW/cm*^{2} at the place of sample location. ±U means the phase sign of lock-in amplifier.

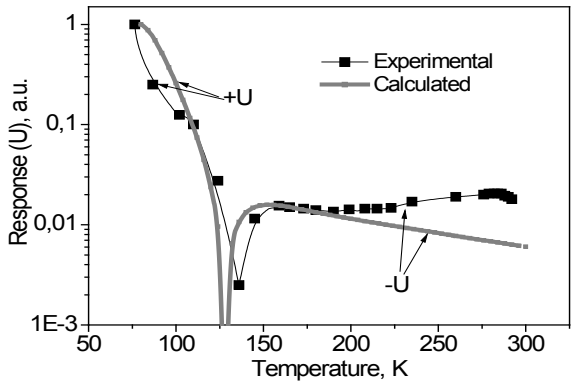

Fig. 7 Response of n-type $Hg_{0.8}Cd_{0.2}Te$ bolometer as a function temperature. ν=37 *GHz*, I_{bias}=1 *mA*. Impurity concentration n~1.5·10^{14} *cm*$^{-3}$, thickness a_l=8 *μm*, width and distance between the contacts are equal to 50 *μm* for experimental and calculated curves. ±U means the phase sign of lock-in amplifier. Parameter which shows the effectiveness of carrier cooling at the contact $q_n=\langle T_{nh}\rangle(0)/\langle T_{nho}\rangle=0.028$ for electrons and $q_p=0$. $\langle T_{nh}\rangle(0)$ is the electron temperature counted from the lattice temperature taking into account cooling at the contact and $\langle T_{nho}\rangle$ is the electron temperature counted from the lattice temperature at stationary and homogeneous heating by radiation.

Use of theoretical model developed above can help qualitatively explain the behavior of response taking into account various components of output signal: Dember effect, thermoelectromotive contribution and free carrier concentration changes. For example, it is seen from Fig. 7 that experimental results and theoretical calculation, that were made by formulas (32, 33), demonstrate good qualitative agreement with position of signal sign inversion (lock-in amplifier) and its temperature dependence.

In Fig. 8 are shown calculated and experimental signal temperature dependences of *p-HgCdTe* layer used as mm-wave warm-electron bolometer. Though the hole concentration values are not coinciding, and the response peak position coincides only qualitively, these depependences show the principle coincidence of theory and experiment – with free hole

carrier concentration increase the response max is shifting toward higher temperatures (at given *ν*).

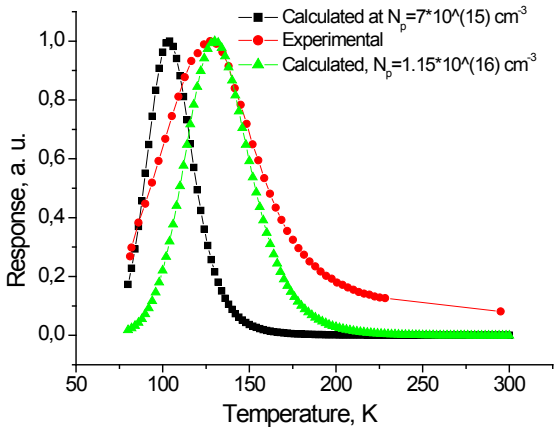

Fig. 8 Calculated and experimental signal temperature dependences at 78 *K* in p-type layer of $Hg_{0.77}Cd_{0.23}Te$. ν=37 *GHz*, I_{bias}=1 *mA*. Impurity concentration is p~$7\cdot10^{15}$ cm^{-3}, thickness a_1=17 *μm*, width a_2=50 *μm* and distance between the contacts are a_3=10 *μm* for experimental and calculated curves. Parameter which shows the effectiveness of carrier cooling at the contact q_n=<T_{nh}>(0)/<T_{nho}>=0.008 for electrons and q_p=0.

In Fig. 9 are shown the NEP values of n- and p-type samples (x~0.2) investigated at T=300 *K* for several radiation frequencies. One can see that the signals depends strongly on radiation frequency. It seems that the mane reason of it are the changes of coupling efficiency because of rather simple antenna used in experiments, as the calculations have shown that there should not be such kind of dependence (see Fig. 3). Similar drop of sensitivity with radiation frequency increase are observed in Schottky-barrier THz detectors [2, 6] and, e.g., in InGaAs broad-band THz sensors [25].

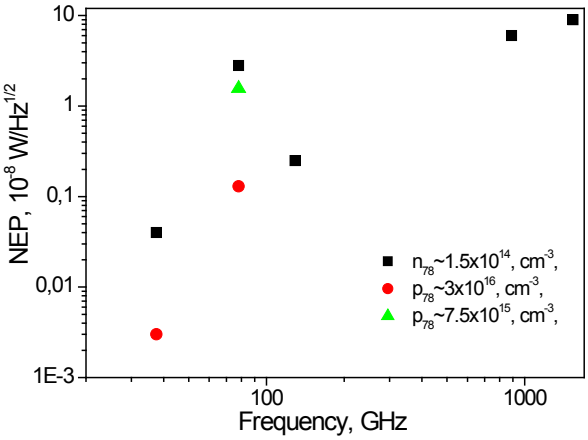

Fig. 9 Estimated NEP values of $Hg_{1-x}Cd_xTe$ (x~0.2) warm electron bolometers at 300 *K*. I_{bias}= 1 *mA*.

In Tab. 1 known NEP data for uncooled mm and sub-mm detectors are compared. As one can see that investigated direct detection HgCdTe bipolar hot-electron bolometers can have NEP comparable with other detectors but these bolometers are much faster that many other ones, and they can be used in some frequency range in arrays, e.g., for active real time imaging.

Detector type	Modulation frequency (Hz)	Operation frequency (THz)	Noise equivalent power (*NEP*), ($W/Hz^{1/2}$)	Refs.
Golay cell	≤ 20	≤ 30	10^{-9}–10^{-10}	Commercial
Piezoelectric	$\leq 10^2$ (decreases with f increasing and depends on dimensions)	≤ 30	$\approx (1–3)\times10^{-9}$ (decreases with ν increase)	Commercial
VO_x microbolometers	$\leq 10^2$	4.3	$>3\ 10^{-10}$ (increases with ν increase)	20
Bi microbolometer	$\leq 10^6$	≤ 3	1.6×10^{-10} (increases with ν increase, degrades in air)	21
Nb microbolometer	–	≤ 30	5×10^{-11}	22
Schottky diodes	$\leq 10^{10}$	≤ 10	$\geq 10^{-10}$ (increases several orders with ν increase within ~ 0.1–10 THz)	6
Si MOSFET	3×10^4	0.645	$\approx 3\times10^{-10}$ (depends on gate length and gate voltage)	23
Si FET	–	≤ 30	$> 10^{-10}$ (depends on gate length and gate voltage)	24
SiN membrane	≤200	≈1.6-4.3	10^{-9}	7
Micro-Golay cell	≤30	0.105	3×10^{-7}	9
HgCdTe HEB	$< 10^8$	≈ 0.03–1.5	~ 4×10^{-10} ($\nu\approx$ 37 GHz, increases with ν increase)	This paper

Tab. 1 Parameters of some uncooled THz wave detectors.

4. Conclusions

Experimental results obtained in the long bipolar bolometer layer approximation confirm the main features of the model proposed. The use of the theoretical model developed, explain the temperature response behavior taking into account various components of output signal: Dember effect, thermoelectromotive contribution and free carrier concentration changes. Under the radiation influence, because of the changes of different signs components contribution and signal registration by lock-in amplifier, the signals registered change their phase. At T=78 *K* under the radiation the sample resistance is decreased in p-type layers, and is increased in n-type layers. The picture is changing to the opposite one under the radiation at room temperature. Under the IR radiation (λ~10 μm) influence the samples resistance is always decreased, as it is connected with interband transitions. Sensitivity of proposed detector was observed in wide spectral range, at least from 0.037 to 1.54 *THz*.

Electron heating by electromagnetic wave in bipolar semiconductor layer opens a perspective for fabrication of THz/sub-THz direct detection bolometers which can be used in multielement arrays as it is done with MCT IR multielement arrays. The opportunity to get acceptable NEP values in multielement structures at room temperature or at moderate cooling, and also relatively short response time (about free carriers life time τ~20-50 *ns* at 300 *K*) are the features of mm/sub-mm bolometer considered.

The parameters of the bolometer considered, which should be optimized by free carrier concentrations, chemical composition, geometrical dimensions and antennas, can be

comparable or better the characteristics of other sub-mm uncooled devices, and they can operate in wide spectral range at moderate cooling conditions.

Appendix 1. Experiment

The layers for bolometers were of *n*- or *p*-type conductivity $Hg_{1-x}Cd_xTe$ bulk layers thinned to a_1~8 μm or liquid phase epitaxial films. They had Au or In electric contacts, which served as antennas. A schematic view of the simplest bolometer design is illustrated in Fig.10.

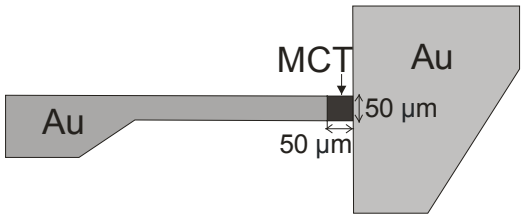

Fig. 10 Schematic drawing of microbolometer design.

Gunn oscillator (ν=75 *GHz*), tunnel diode (ν=37.5 *GHz*), continuously tunable backward-wave oscillators (ν=37.5-53.57, 53.57-78.33, 129.2-142.8 *GHz*), HCN- (ν=0.89 *THz*) and DCN-lasers (ν=1.54 *THz*) were used as THz/sub-THz sources*). Signals from irradiated samples were registered by lock-in amplifier. The radiation was modulated either mechanically or electrically. Modulation frequency was varied between f=0.1 *kHz* and 5 *kHz*. The detectors were fed from a constant current source. The samples were placed to cryostat with teflon window. The radiation was incident on the sample via pyramidal horns. The block-diagram of experimental system is shown in Fig.11.

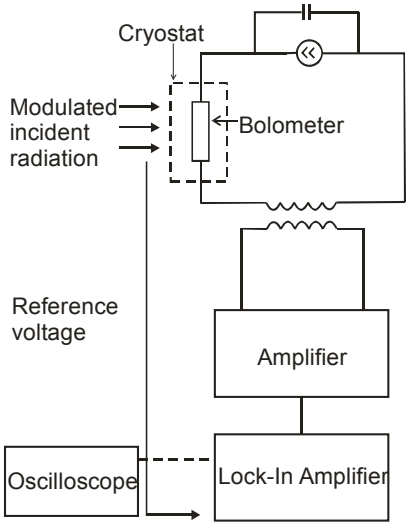

Fig. 11 Block diagram of experimental setup.

Appendix 2. Noise

For $Hg_{1-x}Cd_xTe$ bolometric layers typical are Jonson-Nyquist noise, generation-recombination noise, and additional photon shot noise. The latter one is important in this case

because of high interband absorption (not filtered in these experiments) in narrow-gap MCT photoconductors at hν>0.09 *eV*.

The Johnson-Nyquist mean-square voltage noise

$$\left\langle U_J \right\rangle^2 = 4Rk_B T\Delta f\,, \tag{35}$$

where R is sample resistance, k_B is Boltzmann constant, T is sample temperature, and Δf is bandwidth for central frequency.

The spectral density of generation-recombination noise current caused by interband transitions in semiconductor can be written as [26]

$$S_I(f) = \frac{4I_c^2(b+1)^2 n_0 p_0 \tau}{(bn_0 + p_0)^2 (n_0 + p_0)(1+\omega^2\tau^2)}, \tag{36}$$

where $b=\mu_n/\mu_p$ is the mobility ratio, τ is the dominant lifetime, I_c is the current and n_0 and p_0 refer to the total numbers of electrons and holes in the sample in thermal equilibrium. The values of n_0 and p_0 were found from the intrinsic carrier concentration dependences given, e.g., in [11] for *HgCdTe* semiconductors.

The generation-recombination noise voltage is equal

$$\left\langle U_{g-r} \right\rangle^2 = S_I R^2 \Delta f\,. \tag{37}$$

For photon noise (background photon fluctuation noise) the next expression can be written [27] (for λ=0-14 μm range, where those detectors are sensitive to IR-radiation at detector temperature T=78 *K*)

$$U_{phn} = \left\langle N \right\rangle^{1/2} e\eta AR\,, \tag{38}$$

where N is the photon flux from the T=300 *K* background hemisphere, e is electron charge, η≈0.5 is quantum efficiency of detector, and A is sensitive element area

$$\mathrm{N(T)} = \int_{\lambda_1}^{\lambda_2} \frac{2\pi c}{\lambda^4 \left(e^{\frac{hc}{\lambda kT}} - 1 \right)} d\lambda \tag{39}$$

And total noise

$$U = \sqrt{U_{g-r}^2 + U_J^2 + U_{phn}^2} \tag{40}$$

The noise voltages in the samples were estimated from expressions (35-40) at bandwidth Δf = 1 *Hz*. The results for noise voltages are shown in Tab. 2.

Noise type	*n*-type sample		*p*-type sample	
	T=78 K	T=300 K	T=78 K	T=300 K
Johnson-Nyquist noise, V	$4.2\cdot10^{-10}$	$7\cdot10^{-10}$	$7.1\cdot10^{-10}$	$1.2\cdot10^{-9}$
Generation-recombination noise, V	$1.7\cdot10^{-8}$	$7.2\cdot10^{-10}$	$1.4\cdot10^{-9}$	$2.3\cdot10^{-9}$
Photon noise, V	$3.9\cdot10^{-11}$	$1.1\cdot10^{-11}$	$1.1\cdot10^{-10}$	$3\cdot10^{-11}$
Total noise, V	$1.7\cdot10^{-8}$	$1\cdot10^{-9}$	$1.6\cdot10^{-9}$	$2.6\cdot10^{-9}$

Table 2. Estimated noise voltages.

Estimations of noise level gave the possibility to estimate NEP for these detectors. Taking into account the area of plane contacts as antennas (A= 1.9×10^{-3} cm^{-2}) at ν=37.5 *GHz* for p-type sample (Fig. 5) at T~80-130 *K* the noise equivalent power can reach NEP~5×10^{-12} $W/Hz^{1/2}$. At T=300 *K* for this sample NEP~$3\cdot10^{-11}$ $W/Hz^{1/2}$ (without bias). For shorter wavelengths the NEP values decrease faster than it follows from calculations in Fig. 3, which seems is due to declining of electromagnetic coupling because of simple antenna used.

At ν=0.89 *THz* and T=300 *K* in n-type HgCdTe bolometer NEP≈6×10^{-8} $W/Hz^{1/2}$ (at ν=37.5 *GHz* estimated for similar n-type sample NEP~4×10^{-10} $W/Hz^{1/2}$).

Estimated NEP for n- and p-type samples are shown in Fig. 9 in dependence of radiation frequency.

Rather similar radiation frequency sensitivity dependence (sensitivity drastically dropping down at ν>1.4 *THz* from S_v~1 *V/W* to S_v~3×10^{-2} *V/W*) was observed in bow-tie InGaAs room-temperature THz sensor [25].

Authors are thankful to Yu. Kamenev for response measuring at *ν*=0.89 *THz* and *ν*=1.54 *THz*.

References

[1] S. Hargreaves and R. A. Lewis, Terahertz imaging: Materials and methods, *J. Mater. Sci.: Mater. Electron.* 18, S299–S303, (2007).

[2] T. W. Crowe, W. L. Bishop, D. W. Porterfield, J. L. Hesler and R. M. Weikle, Opening the terahertz window with integrated diode circuits, *IEEE J. Solid-State Circuits,* 40, 2104-2110, (2005).

[3] M. Tonouchi, Galore new applications of terahertz science and technology, *Terahertz Science and Technology*, 2, 90-101, (2009).

[4] J. Zmuidzinas and P. L. Richards, Superconducting detectors and mixers for millimeter and submillimeter astrophysics, *Proc. IEEE,* 92, 1597-1616, (2004).

[5] F. Sizov, THz radiation sensors, *Opto-Electronics Review*, 17, 10-36, (2010).

[6] V. G. Bozhkov, Semiconductor detectors, mixers, and frequency multipliers for the terahertz band, *Radiophys. Quant. Electr.*, 46, 631-656, (2003).

[7] I. Kasalynas, A. J. L. Adam, T. O. Klaassen, J. N. Hovenier, G. Pandraud, V. P. Iordanov, and P. M. Sarro, Design and Performance of a Room-Temperature Terahertz Detection Array for Real-Time Imaging, *IEEE J. Selected Topics Quant. Electr.*, 14, 363-369, (2008).

[8] W. Knap, M. Dyakonov, D. Coquillat, F. Teppe, N. Dyakonova, J. Łusakowski, K. Karpierz, M. Sakowicz, G. Valusis, D. Seliuta, I. Kasalynas, A. El Fatimy, Y. M. Meziani, and T. Otsuji, "Field effect transistors for terahertz detection: physics and first imaging applications," *J. IR MM THz Waves* 30, 1319–1337, (2009).

[9] D. Denison, M. Knotts, M. McConney, V. Tsukruk, Experimental characterization of mm-wave detection by a micro-array of Golay cells, *Proc. SPIE*, 7309, 73090J, (2009).

[10] A. Lisauskas, U. Pfeiffer, E. Öjefors, P. Haring Bolivar, D. Glaab, and H. G. Roskos, Rational design of high-responsivity detectors of THz radiation based on distributed self-mixing in silicon CMOS transistors, *J. Appl. Phys*., 105, 114511, (2009).

[11] A. Rogalski, Infrared detectors, *Gordon and Breach, The Netherlands*, (2000).

[12] A. Betz, R. Boreiko, Y. Zhou, J. Zhao, Y. Selamet, Y. Chang, R. Ashokan, C. Bucker, S. Sivananthan, HgCdTe Photoconductive Mixers for 3-5 THz, *Proceedings of 14th International Simposium on Space Terahertz Technology, Tucson, Arisona*, 102-111, (2003).

[13] C. Stellmach, R. Bonk, A. Vasilyev, A. Hirsch, C. R. Becker, G. Nachtwei, Terahertz photoconductivity in GaAs/AlGaAs and HgTe/HgCdTe quantum Hall devices, *Phys. Status Solidi*, C3, 2510-2513, (2007).

[14] B. V. Rollin, Detection of millimetre and sub-millimetre wave radiation by free carrier absorption in a semiconductor, *Proc. Phys. Soc*., 77, 1102-1103, (1961).

[15] M. A. Kinch, B. V. Rollin, Detection of millimetre and sub-millimetre wave radiation by free carrier absorption in a semiconductor, *Brit. J. Appl. Phys*., 14, 672-676, (1963).

[16] V. Dobrovolsky, F. Sizov, A room temperature, or moderately cooled, fast THz semiconductor hot electron bolometer, *Semicond. Sci. Technol*., 22, 103-106, (2007).

[17] K. Seeger, *Semiconductor physics, Wien, Springer*, (1973).

[18] A. V. Ljubchenko, E. A. Salkov and F. F. Sizov, *Physical basis of semiconductor infrared photoelectronics, Kiev, Naukova dumka*, in Russian, (1984).

[19] D. G. Ikusov, F. F. Sizov, S. V. Stariy, V. V. Teterkin. Mechanisms of recombination of nonequilibrium charge carriers in epitaxial $Cd_xHg_{1-x}Te$ (x=0.20–0.23) layers, *Semiconductors,* 41, 130-135, (2007).

[20] A. W. M. Lee, B. S. Williams, S. Kumar, Q. Hu, and J. L. Reno, Real-time imaging using a 4.3-THz quantum cascade laser and a 320x240 microbolometer focal-plane array, *IEEE Photonics Techn. Lett*. 18, 1415-1417, (2006).

[21] T.-L. Hwang, S. E. Scharz, and D. B. Rutledge, Microbolometers for infrared detection, *Appl. Phys. Lett*. 34, 773–776, (1979).

[22] E. N. Grossman and A. J. Miller, Active millimeter-wave imaging for concealed weapons detection, *Proc. SPIE* 5077, 62–70, (2003).

[23] A. Lisauskas, D. Glaab, H. G. Roskos, E. U. Oejefors, and R. Pfeiffer, Terahertz imaging with Si MOSFET focal-plane arrays, *Proc. SPIE* 7215, 72150J, (2009).

[24] R. Tauk, F. Teppe, S. Boubanga, D. Coquillat, and W. Knap, Y. M. Meziani, C. Gallon, F. Boeuf, T. Skotnicki, and C. Fenouillet-Beranger, Plasma wave detection of terahertz radiation by silicon field effects transistors: Responsivity and noise equivalent power, *Appl. Phys. Lett*. 89, 253511, (2006).

[25] D. Seliuta, I. Kasalynas, V. Tamosiunas, S. Balakauskas, Z. Martunas, S. Asmontas, G. Valusis, A. Lisauskas, H.G. Roskos, and K. Kohler, Silicon lens-coupled bow-tie InGaAs-based broadband terahertz sensor operating at room temperature, *Electron. Lett*., 42, 825-827, (2006).

[26] K. M. Van Vliet, Noise Limitations in Solid State Photodetectors, *Appl. Optics*, 6, 1145-1169, (1967).

[27] N. B. Lukyanchikova, Noise research in semiconductor physics, *Gordon and Breach Science Publishers, Amsterdam*, (1999).